

# Topological axion states in magnetic insulator $\text{MnBi}_2\text{Te}_4$ with the quantized magnetoelectric effect

Dongqin Zhang,<sup>1,2</sup> Minji Shi,<sup>1,2</sup> Dingyu Xing,<sup>1,2</sup> Haijun Zhang,<sup>1,2,\*</sup> and Jing Wang<sup>3,2,4,†</sup>

<sup>1</sup>*National Laboratory of Solid State Microstructures,*

*School of Physics, Nanjing University, Nanjing 210093, China*

<sup>2</sup>*Collaborative Innovation Center of Advanced Microstructures, Nanjing University, Nanjing 210093, China*

<sup>3</sup>*State Key Laboratory of Surface Physics, Department of Physics, Fudan University, Shanghai 200433, China*

<sup>4</sup>*Institute for Nanoelectronic Devices and Quantum Computing, Fudan University, Shanghai 200433, China*

(Dated: May 2, 2022)

Topological states of quantum matter have attracted great attention in condensed matter physics and materials science [1–4]. The study of time-reversal-invariant (TRI) topological states in quantum materials has made tremendous progress in both theories and experiments [5–24]. As a great success, thousands of TRI topological materials are predicted through sweeping search [25–27]. Richer exotic phenomena are expected to appear in magnetic topological materials because of varied magnetic configurations, but this study falls much behind due to the complex magnetic structures and transitions [28–33]. Here, we predict the tetradymite-type compound  $\text{MnBi}_2\text{Te}_4$  and its related materials host interesting magnetic topological states. The magnetic ground state of  $\text{MnBi}_2\text{Te}_4$  is an antiferromagnetic phase which leads to an antiferromagnetic topological insulator state with a large topologically non-trivial energy gap ( $\sim 0.2$  eV). It is the parent state for the axion state, which has gapped bulk and surface states, and quantized topological magnetoelectric effect. The ferromagnetic phase of  $\text{MnBi}_2\text{Te}_4$  leads to an ideal minimal type-II Weyl semimetal with two Weyl points accompanied by one hole-type and one electron-type Fermi pocket at the Fermi level, which has never been discovered elsewhere. We further present a simple and unified continuum model to capture the salient topological features of this kind of materials.

The recent discovery of the TRI topological insulator brings the opportunity to realize a large family of exotic topological phenomena in which the topological gapless surface states are magnetically gapped [34]. Tremendous efforts have been made to introduce magnetism into TRI topological insulators. Most successful example is the first realization of the quantum anomalous Hall (QAH) effect in Cr-doped  $(\text{Bi,Sb})_2\text{Te}_3$  topological insulator thin films [28, 35]. Aside from the dilute magnetic topological insulators, intrinsic magnetic materials expect to provide a clean platform to study magnetic topological states with new interesting topological phenomena. Some magnetic topological states have been theoretically proposed [36], such as antiferromagnetic topological insulator [29], dynamical axion field [37], magnetic Dirac semimetal [32, 33, 38, 39], and magnetic Weyl semimetals [30, 31, 40]. Unfortunately, none of them have been realized in experiments. Therefore, realistic magnetic topological materials are highly desired. The class of materials predicted in this letter provide an ideal platform for emergent magnetic topological phenomena, such as, the antiferromagnetic topological insulator, the topological axion state with quantized topological magnetoelectric effect, the ideal minimum type-II Weyl semimetal, the QAH effect, two-dimensional ferromagnetism and so on.

*Electronic structure.* The tetradymite-type compounds  $\text{XA}_2\text{B}_4$ , also written as  $\text{XB}\cdot\text{A}_2\text{B}_3$  with  $\text{X} = \text{Ge}, \text{Sn}, \text{Pb}$  or  $\text{Mn}$ ,  $\text{A} = \text{Sb}$  or  $\text{Bi}$ , and  $\text{B} = \text{Se}$  or  $\text{Te}$ , crystallize in a rhombohedral crystal structure with the space group  $D_{3d}^5$  (No. 166) with seven atoms in one unit cell.

We take  $\text{MnBi}_2\text{Te}_4$  as an example, which has been successfully synthesized in experiments [41], and show its crystal structure in Fig. 1. It has layered structures with a triangle lattice. The trigonal axis (three-fold rotation symmetry) is defined as the  $z$  axis, a binary axis (two-fold rotation symmetry) is defined as the  $x$  axis and a bisectrix axis (in the reflection plane) is defined as the  $y$  axis for the coordinate system. The material consists of seven-atom layers (e.g.  $\text{Te1-Bi1-Te2-Mn-Te3-Bi2-Te4}$ ) arranged along the  $z$  direction, known as a septuple layer, which could also be simply viewed as the intergrowth of (111) plane of rock-salt structure  $\text{MnTe}$  within the quintuple layer of topological insulator  $\text{Bi}_2\text{Te}_3$  (see Fig. 1a and c) [10]. The coupling is strong between neighbor atomic layers within each septuple layer but much weaker, predominantly of the van der Waals type, between different septuple layers. The Mn site has the role of an inversion centre, and the existence of inversion symmetry enables us to construct eigenstates with definite parity for this system.

Isolated Mn atom has electron configuration  $3d^54s^2$ . Based on first-principles calculations, we find that each Mn atom in  $\text{MnBi}_2\text{Te}_4$  tends to lose two electrons and interestingly have half filled  $d$  orbitals. So  $\text{MnBi}_2\text{Te}_4$  is expected to form the magnetic ground state similar to the antiferromagnetic  $\text{MnTe}$ . In a previous work, the  $\text{MnBi}_2\text{Te}_4$  septuple layer is predicted to be ferromagnetic with the out-of-plane easy axis [42]. We performed total energy calculations on different magnetic phases for the three-dimensional bulk  $\text{MnBi}_2\text{Te}_4$ , and the results are listed in Fig. 1e. Our calculations show that the A-

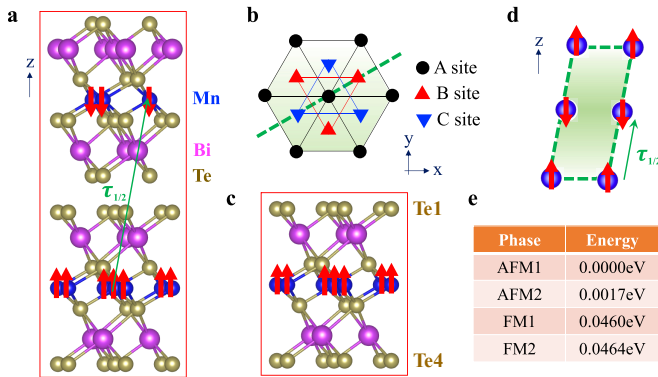


FIG. 1. Crystal structure and magnetic structure. **a**, The unit cell of antiferromagnetic  $\text{MnBi}_2\text{Te}_4$  consists of two septuple layers. The red arrows represent the spin moment of Mn atom. The green arrow denotes for the half translation operator  $\tau_{1/2}$ . **b**, Schematic top view along the  $z$ -direction. The triangle lattice in one septuple layer has three different positions, denoted as A, B and C. The dotted green line is used for the (011) plane. **c**, The unit cell of ferromagnetic  $\text{MnBi}_2\text{Te}_4$  has one septuple layer, and Mn sites have the role of inversion centers. **d**, The schematic of the (011) plane, with the blue balls denoting Mn atoms. **e**, The total energy for different magnetic ordered states obtained from first-principles calculations. The A-type AFM1 state has the lowest total energy.

type antiferromagnetic phase with the out-of-plane easy axis, denoted as AFM1 (seen in Fig. 1a), is the magnetic ground state. It is ferromagnetic within the  $xy$  plane in each septuple layer, consisting with the previous report [42], and antiferromagnetic between neighbor septuple layers along the  $z$  direction. The total energy of the A-type antiferromagnetic phase AFM2 with the in-plane easy axis is slightly higher than that of AFM1, and lower than that of ferromagnetic phase FM1 with the out-of-plane easy axis, which indicates that the magnetic anisotropy is weaker than the effective magnetic exchange interaction between Mn atoms in neighbor septuple layers. The ferromagnetic phase FM2 with in-plane easy axis has the highest energy. In the following discussion, we would focus on the AFM1 (the magnetic ground state) and FM1 (realized through an external magnetic field) states.

Firstly we study the magnetic ground state with the AFM1 order. The unit cell consists of two septuple layers, two times of that in the FM1 state. The time-reversal symmetry  $\Theta$  is broken, however, a combined symmetry  $\mathcal{S} = \Theta\tau_{1/2}$  is preserved, where  $\tau_{1/2}$  is the half translation operator connecting nearest spin-up and -down Mn atomic layers, marked in Fig. 1a. The antiunitary operator  $\mathcal{S}$  could also lead to a  $\mathcal{Z}_2$  topological invariant [29], which is well defined on the Brillouin-zone plane with  $\mathbf{k} \cdot \tau_{1/2} = 0$ . The band structures of AFM1 state without and with spin-orbit coupling (SOC) are shown in Fig. 2a and b, respectively. The system has a large energy gap of

about 0.2 eV. One can also see the anti-crossing feature around the  $\Gamma$  point from the band inversion, suggesting that  $\text{MnBi}_2\text{Te}_4$  might be topologically nontrivial. Since the inversion symmetry  $\mathcal{I}$  is still preserved, the parity is well defined all time-reversal-invariant momenta (TRIM)  $\Gamma(0, 0, 0)$ ,  $F(\pi, \pi, 0)$ ,  $L(\pi, 0, 0)$ ,  $Z(\pi, \pi, \pi)$  in the Brillouin zone, and the Fu and Kane method [43] is employed to calculate the  $\mathcal{Z}_2$  invariant. Here we only need consider the TRIM with  $\bar{\mathbf{G}} \cdot \tau_{1/2} = n\pi$ , which are four momenta ( $\Gamma$  and three  $F$ ). As expected, by turning on SOC, the parity of one occupied band is changed at  $\Gamma$  point from the band inversion between the  $|P1_z^+\rangle$  of Bi and the  $|P2_z^-\rangle$  of Te, schematically shown in Fig. 2d, whereas the parity remains unchanged for all occupied bands at the three momenta  $F$  (see Fig. 2e), so the  $\mathcal{Z}_2$  invariant is calculated to be 1, concluding that antiferromagnetic  $\text{MnBi}_2\text{Te}_4$  is an antiferromagnetic topological insulator, which is the parent state for the topological axion state.

The existence of topological surface states is one of the most important properties of the topological insulators. However, the topological insulator state in antiferromagnetic  $\text{MnBi}_2\text{Te}_4$  protected by  $\mathcal{S}$  symmetry is topological in a weaker sense than the strong topological insulator protected by  $\Theta$  symmetry, which manifests in that the existence of gapless surface state depends on the surface plane. As shown in Fig. 4a, there is no gapless surface states on the (111) surface, for  $\mathcal{S}$  symmetry is broken. Only on the  $\mathcal{S}$  symmetry preserving surfaces such as (011) surface, the gapless surface states are topological protected. As shown in Fig. 4b, topological surface state forms a single Dirac-cone-type dispersion at the  $\Gamma$  point on the (011) surface.

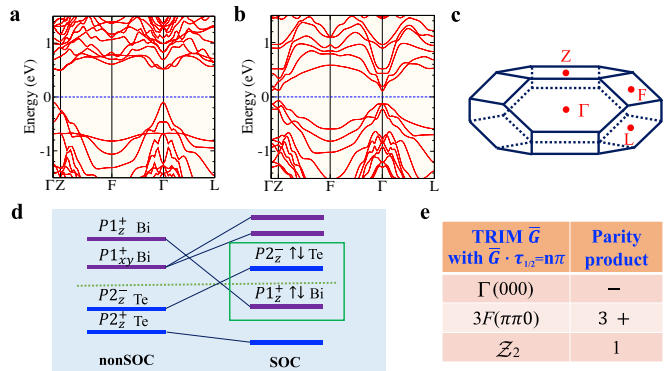


FIG. 2. Electronic structure of AFM1  $\text{MnBi}_2\text{Te}_4$ . **a, b**, The band structure of AFM1 state without (a) and with (b) SOC. **b**, The bands are two-fold degenerate due to conserved  $\mathcal{I}$  and  $\mathcal{S}$ . **c**, Brillouin zone for  $\text{MnBi}_2\text{Te}_4$  with space group  $R\bar{3}m$ . The four inequivalent TRIM are  $\Gamma(0, 0, 0)$ ,  $L(\pi, 0, 0)$ ,  $F(\pi, \pi, 0)$  and  $Z(\pi, \pi, \pi)$ . **d**, Schematic diagram of the band inversion at the  $\Gamma$  point. The green dashed line represents the Fermi level. **e**, The parity product at the TRIM ( $\Gamma$  and  $3F$ ) with  $\bar{\mathbf{G}} \cdot \tau_{1/2} = n\pi$ . The parity product is ‘-’ at  $\Gamma$  point due to the band inversion, and the topological invariant  $\mathcal{Z}_2$  is 1.

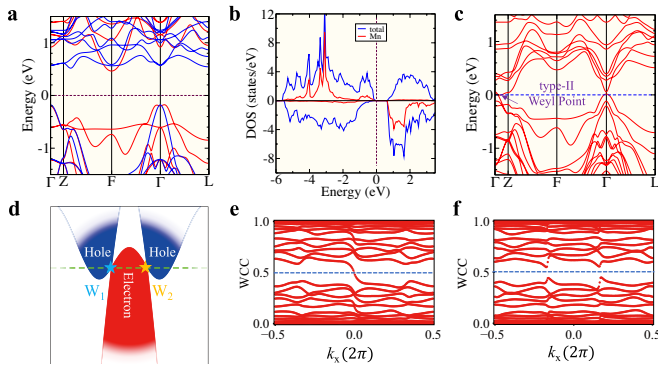


FIG. 3. Electronic structure of FM1  $\text{MnBi}_2\text{Te}_4$ . **a**, **c**, Band structure for FM1 state without (**a**) and with (**c**) SOC. The dashed line indicates the Fermi level. In (**a**), the red/blue lines are spin-up/-down bands. **b**, The density of states (DOS) without SOC. The red line is the partial DOS of Mn atoms, indicating a high-spin state. **c**, There exists only two type-II Weyl points with opposite monopole charges at the Fermi level along  $\Gamma$ - $Z$  line. **d**, The schematic of the two ideal type-II Weyl points (W1 and W2) in the ‘ $-Z$ - $\Gamma$ - $Z$ ’ line. **e**, **f**, The evolution of Wannier charge centers (WCC) along the  $k_x$  direction in the  $k_z = 0$  plane (**e**) and in the  $k_z = \pi$  plane (**f**). The WCCs cross the reference horizontal line once in (**e**), indicating the Chern number  $C = 1$  in the  $k_z = 0$  plane. Oppositely, the WCCs don’t cross the reference line in (**f**), indicating the Chern number  $C = 0$  in the  $k_z = \pi$  plane.

Then the electronic structure of FM1 state is investigated. The moment per Mn atom is found to  $\sim 4.2 \mu_B$ . Fig. 3a and c show the band structure of  $\text{MnBi}_2\text{Te}_4$  without and with the SOC effect, respectively. By comparing the two figure parts, one can see that the only qualitative change induced by turning on the SOC effect is an anti-crossing feature around the  $\Gamma$  point, which thus indicates a band inversion between the conduction and valence bands, similar to that in TRI topological insulator  $\text{Bi}_2\text{Se}_3$  [10]. Different from topological insulators, two ideal type-II Weyl points appear along the ‘ $-Z$ - $\Gamma$ - $Z$ ’ line. For example, one Weyl point is clearly seen between  $\Gamma$  and  $Z$  in the band structure of Fig. 3c. This is the first discovered minimal Weyl semimetal system with two ideal type-II Weyl points at the Fermi level in realistic materials, schematically shown in Fig. 3d. There is only one hole-type pocket and one electron-type pocket accompanying each type-II Weyl point. In order to confirm the topological property, the Willson loop [44] is calculated in  $k_z = 0$  and  $k_z = \pi$  planes, as shown in Fig. 3e and f, respectively. One can see that the Chern number  $C$  is 1 at the  $k_z = 0$  plane, and 0 at the  $k_z = \pi$  plane, which is consistent with the Weyl semimetal band structure. Furthermore, the surface states of FM1 state on different typical surfaces are calculated. In Fig. 4c, there is no

opened Fermi arc on the (111) surface, for the two Weyl points are exactly projected to the surface  $\bar{\Gamma}$  point. While in Fig. 4d and e, one can see the surface Fermi arcs on the (011) surface connect to the Weyl points with a long length ( $\sim 0.35 \text{ \AA}^{-1}$ ), and the two type-II Weyl points are also well separated ( $\sim 0.10 \text{ \AA}^{-1}$ ) along the  $k_z$  direction. When  $\text{MnBi}_2\text{Te}_4$  with FM1 phase is fabricated into thin film, it is expected to realize the QAH state.

*Low-energy effective model.* As the topological nature is determined by the physics near the  $\Gamma$  point, a simple effective Hamiltonian can be written down to characterize the low-energy long-wavelength properties of the system. We start from the four low-lying states  $|P1_z^+, \uparrow(\downarrow)\rangle$  and  $|P2_z^-, \uparrow(\downarrow)\rangle$  at the  $\Gamma$  point. Here the superscripts ‘+’, ‘-’ stand for the parity of the corresponding states. Without the SOC effect, around the Fermi energy, the bonding state  $|P1_z^+\rangle$  of two Bi layers stays above of the antibonding state  $|P2_z^-\rangle$  of two Te layers (Te1 and Te4 in septuple layers). As shown in Fig. 3d, the SOC mixes spin and orbital angular momenta while preserving the total angular momentum, and  $|P1_z^+, \uparrow(\downarrow)\rangle$  state is pushed down and the  $|P2_z^-, \uparrow(\downarrow)\rangle$  state is pushed up, leading to the band inversion and parity exchange. Now the effective Hamiltonian can be constructed by the theory of invariants for the finite wave vector  $\mathbf{k}$ . In the nonmagnetic state, the important symmetries of the system are

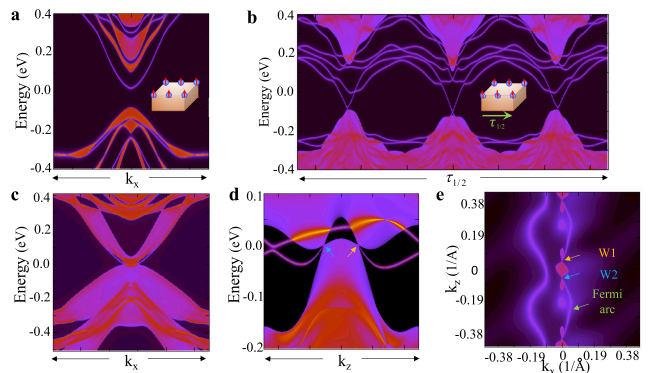


FIG. 4. Surface states. **a**, **b**, Energy and momentum dependence of the local density of states (LDOS) for AFM1 phase on the (111) and (011) surfaces, respectively. In **a**, The surface states on (111) surface are fully gapped due to the  $\mathcal{S}$  symmetry broken. **b**, The gapless surface states can be seen at the  $\Gamma$  point with a linear dispersion in the bulk gap on the  $\mathcal{S}$ -preserving (011) surface. **c**, **d**, Energy and momentum dependence of the LDOS for FM1 phase on the (111) and (011) surfaces, respectively. In **d**, the two Weyl points are separated along the  $k_z$  direction of about  $0.1 \text{ \AA}^{-1}$ . **e**, The corresponding Fermi surface on the (011) plane of FM1 phase. There are two Fermi arcs connecting the Weyl points W1 and W2. The hole-type and electron-type bulk Fermi pockets accompany with the type-II Weyl points.

time-reversal symmetry  $\Theta$ , inversion symmetry  $\mathcal{I}$ , three-fold rotation symmetry  $C_{3z}$  along the  $z$  axis and two-fold rotation symmetry  $C_{2x}$  along the  $x$  axis. In the basis of ( $|P1_z^+, \uparrow\rangle$ ,  $|P2_z^-, \uparrow\rangle$ ,  $|P1_z^+, \downarrow\rangle$ ,  $|P2_z^-, \downarrow\rangle$ ), the representation of the symmetry operations is given by  $\Theta = 1_{2 \times 2} \otimes i\sigma^y \mathcal{K}$ ,  $\mathcal{I} = \tau^z \otimes 1_{2 \times 2}$ ,  $C_{3z} = \exp(1_{2 \times 2} \otimes i(\pi/3)\sigma^z)$  and  $C_{2x} = \exp(1_{2 \times 2} \otimes i(\pi/2)\sigma^x)$ , where  $\mathcal{K}$  is the complex conjugation operator,  $\sigma^{x,y,z}$  and  $\tau^{x,y,z}$  denote the Pauli matrices in the spin and orbital space, respectively. By requiring these four symmetries and keeping only the terms up to quadratic order in  $\mathbf{k}$ , we obtain the following generic form of the effective Hamiltonian for nonmagnetic state,

$$\mathcal{H}_{\text{NM}}(\mathbf{k}) = \epsilon_0(\mathbf{k}) + \begin{pmatrix} M_\gamma(\mathbf{k}) & A_1 k_z & 0 & A_2 k_- \\ A_1 k_z & -M_\gamma(\mathbf{k}) & A_2 k_- & 0 \\ 0 & A_2 k_+ & M_\gamma(\mathbf{k}) & -A_1 k_z \\ A_2 k_+ & 0 & -A_1 k_z & -M_\gamma(\mathbf{k}) \end{pmatrix}, \quad (1)$$

where  $k_\pm = k_x \pm ik_y$ ,  $\epsilon_0(\mathbf{k}) = C + D_1 k_z^2 + D_2(k_x^2 + k_y^2)$  and  $M_\gamma(\mathbf{k}) = M_0^\gamma + B_1^\gamma k_z^2 + B_2^\gamma(k_x^2 + k_y^2)$ .

The FM1 state breaks  $\Theta$  and  $C_{2x}$  but preserves the combined  $C_{2x}\Theta$ , therefore the effective Hamiltonian for FM1 is obtained by adding perturbative term  $\delta\mathcal{H}_{\text{FM1}}(\mathbf{k})$  respecting the corresponding symmetries into  $\mathcal{H}_{\text{NM}}(\mathbf{k})$ , which is

$$\delta\mathcal{H}_{\text{FM1}}(\mathbf{k}) = \begin{pmatrix} M_1(\mathbf{k}) & A_3 k_z & 0 & A_4 k_- \\ A_3 k_z & M_2(\mathbf{k}) & -A_4 k_- & 0 \\ 0 & -A_4 k_+ & -M_1(\mathbf{k}) & A_3 k_z \\ A_4 k_+ & 0 & A_3 k_z & -M_2(\mathbf{k}) \end{pmatrix}, \quad (2)$$

where  $M_{1,2}(\mathbf{k}) = M_\alpha(\mathbf{k}) \pm M_\beta(\mathbf{k})$ , and  $M_j(\mathbf{k}) = M_0^j + B_1^j k_z^2 + B_2^j(k_x^2 + k_y^2)$  with  $j = \alpha, \beta$ . By fitting the energy spectrum of the effective Hamiltonian with that of the first-principles calculation, the parameters in the effective model can be determined, which can be found in the Methods section. The  $M_{1,2}$  terms characterize the Zeeman coupling with the magnetized Mn orbitals, and in general  $M_1 \neq M_2$  denotes the different effective  $g$ -factor of  $|P1_z^+, \uparrow(\downarrow)\rangle$  and  $|P2_z^-, \uparrow(\downarrow)\rangle$ .

The AFM1 state breaks  $\Theta$  but preserves  $\mathcal{S} = 1_{2 \times 2} \otimes i\sigma^y \mathcal{K} e^{i\mathbf{k} \cdot \boldsymbol{\tau}_{1/2}}$ , and the unit cell doubles compared to FM1 state. One can construct the effective Hamiltonian for AFM1 from the model for FM1 state by considering two septuple layers with opposite magnetization, which will include eight bands. For simplicity, we obtain the four-band model similar to the above analysis. From band structure analysis, the four bands close the Fermi energy in the AFM1 state are the new bonding state  $|P1_z^+, \uparrow(\downarrow)\rangle$  of four Bi layers and the antibonding state  $|P2_z^-, \uparrow(\downarrow)\rangle$  of four Te layers (two Te1 and two Te4 in neighboring septuple layers). In the basis of ( $|P1_z^+, \uparrow\rangle$ ,  $|P2_z^-, \uparrow\rangle$ ,  $|P1_z^+, \downarrow\rangle$ ,  $|P2_z^-, \downarrow\rangle$ ), by requiring the symmetries  $\mathcal{I}$ ,  $C_{3z}$  and  $\mathcal{S}$ , we get the effective Hamiltonian for AFM1 which has the same expression as  $\mathcal{H}_{\text{NM}}(\mathbf{k})$  but with different param-

eters, namely

$$\mathcal{H}_{\text{AFM1}}(\mathbf{k}) = \epsilon'_0(\mathbf{k}) + \begin{pmatrix} M'(\mathbf{k}) & A'_1 k_z & 0 & A'_2 k_- \\ A'_1 k_z & -M'(\mathbf{k}) & A'_2 k_- & 0 \\ 0 & A'_2 k_+ & M'(\mathbf{k}) & -A'_1 k_z \\ A'_2 k_+ & 0 & -A'_1 k_z & -M'(\mathbf{k}) \end{pmatrix}, \quad (3)$$

where  $\epsilon'_0(\mathbf{k}) = C' + D'_1 k_z^2 + D'_2(k_x^2 + k_y^2)$  and  $M'(\mathbf{k}) = M'_0 + B'_1 k_z^2 + B'_2(k_x^2 + k_y^2)$ . The fitting parameters are listed in the Methods section. We notice that  $M'_0 < 0$  and  $B'_1, B'_2 > 0$ , which correctly characterizes the band inversion around  $\mathbf{k} = 0$  and the topologically non-trivial nature of the system. The model in Eq. (3) is the same as the model for 3D topological insulator in  $\text{Bi}_2\text{Te}_3$  [10], and the 2D band inversion remains when thin film  $\text{MnBi}_2\text{Te}_4$  with AFM1 phase exceeds 4 septuple layers. Interestingly, for thickness with even number of septuple layers larger than four, although band inversion exists, the Chern number is zero due to conserved  $\mathcal{I}\Theta$ . For thickness with odd number of septuple layers larger than 4,  $\Theta\mathcal{I}$  is also broken and the system has spin polarized band inversion, which lead to QAH effect.

*Axion state and topological response.* The AFM1  $\text{MnBi}_2\text{Te}_4$  is the parent state for topological axion state. Such axion state has gapped bulk and surface states, and nonzero topological electromagnetic response described by the topological  $\theta$  term,  $S_\theta = (\theta/2\pi)(\alpha/2\pi) \int d^3x dt \mathbf{E} \cdot \mathbf{B}$ . Here,  $\mathbf{E}$  and  $\mathbf{B}$  are the conventional electromagnetic fields inside the insulator,  $\alpha = e^2/\hbar c$  is the fine-structure constant,  $e$  is the charge of an electron, and  $\theta$  is the dimensionless pseudoscalar parameter describing the axion insulator. The axion state can be obtained by gapping all the  $\mathcal{S}$ -preserving surfaces from AFM1 state, which can be simply obtained by growing realistic materials without any  $\mathcal{S}$ -preserving surfaces or applying a small in plane magnetic field. Physically,  $\theta$  has an explicit microscopic expression of the momentum space Chern-Simons form [34]

$$\theta = \frac{1}{4\pi} \int d^3k \epsilon^{ijk} \text{Tr} \left[ \mathcal{A}_i \partial_j \mathcal{A}_k + i \frac{2}{3} \mathcal{A}_i \mathcal{A}_j \mathcal{A}_k \right], \quad (4)$$

where  $\partial_j = \partial/\partial k_j$ ,  $\mathcal{A}_i^{\mu e}(\mathbf{k}) = -i \langle u_{\mathbf{k}}^\mu | \partial_i | u_{\mathbf{k}}^e \rangle$  is the momentum space non-abelian gauge field, with  $|u_{\mathbf{k}}^\mu\rangle$  and  $|u_{\mathbf{k}}^e\rangle$  referring to the periodic part of the Bloch function of the occupied bands. All physical quantities in the bulk depend on  $\theta$  only modulo  $2\pi$ . As  $\theta$  is odd under time-reversal and parity operation, only time-reversal and parity-breaking perturbations can induce a change of  $\theta$ . The Mn sites always act as the inversion center, therefore,  $\theta$  of the axion state is the same as that of AFM1 state, where  $\theta = \pi$  is guaranteed by the  $\mathcal{S}$  symmetry. Such axion state emerged in  $\text{MnBi}_2\text{Te}_4$  provides an ideal platform for quantized topological magnetoelectric effect [34, 45], which has not been experimentally observed, and is different from proposed axion state in the ferromagnet-topological insulator het-



erostucture where the gapless surface states on side surfaces are hard to eliminate [45–48]. Experimentally, such quantized topological magnetoelectric effect can be observed by measuring the induction of a parallel polarization current when an ac magnetic field is applied [45], which is  $\mathcal{J} = (\theta/\pi)(e^2/2h)(\partial B_x/\partial t)\ell d$ . Here,  $d$  and  $\ell$  are the thickness and width of the  $\text{MnBi}_2\text{Te}_4$  sample. For an estimation, taking  $B_x = B_0 e^{-i\omega t}$ ,  $B_0 = 10$  G,  $\omega/2\pi = 1$  GHz,  $d = 50$  nm,  $\theta = \pi$ , and  $\ell = 400$   $\mu\text{m}$ , we have  $\mathcal{J} = -i\mathcal{J}_0 e^{-i\omega t}$  with  $\mathcal{J}_0 = 2.22$  nA, in the range accessible by experiments.

It is worth mentioning that the Néel order in AFM1 state is quite different from the Néel order in the dynamical axion field proposed in Ref. [37]. In the latter case, the Néel order breaks the time-reversal symmetry  $\Theta$  and parity  $\mathcal{I}$ , but conserves  $\mathcal{I}\Theta$ . The magnetic fluctuation of the Néel order leads to linear contribution to the fluctuation of axion field, and the static  $\theta$  deviates from  $\pi$ . While in the former case, the Néel order conserves  $\mathcal{I}$  and  $\mathcal{S}$ , thus the static  $\theta = \pi$ , and to the linear order, the magnetic fluctuation has no contribution to the dynamics of axion field.

*Materials.* Other tetradymite-type compounds  $\text{XBi}_2\text{Te}_4$ ,  $\text{XBi}_2\text{Se}_4$  and  $\text{XSb}_2\text{Te}_4$  (X is Mn and Eu), if with the same rhombohedral crystal structure, are also promising candidates to host magnetic topological states similar to  $\text{MnBi}_2\text{Te}_4$ . Actually, tetradymite-type compounds  $\text{XB}\cdot\text{A}_2\text{B}_3$  belong to a large class of ternary chalcogenides materials  $(\text{XB})_n\cdot(\text{A}_2\text{B}_3)_m$  with X = (Ge, Sn or Pb), A = (Sb or Bi) and B = (Se or Te), most of which were found to be topological insulators [49]. Interestingly,  $(\text{GeTe})_n(\text{Sb}_2\text{Te}_3)_m$  and  $(\text{GeTe})_n(\text{Bi}_2\text{Te}_3)_m$  have been widely studied as phase change memory materials [50]. By tuning the layer index  $m$  and  $n$ , we can control the crystal structure, the topological property, and the magnetic property of the series of materials  $(\text{XB})_n\cdot(\text{A}_2\text{B}_3)_m$ , which opens a broad way to study emergent phenomena of magnetic topological states.

*First-principles calculations of electronic and magnetic properties.* The first-principles calculations are carried out in the framework of the local-density approximations (LDA) approximation of the density functional theory through employing the Vienna ab initio simulation package (VASP) with projector augmented wave pseudopotentials [51, 52]. The lattice constant (FM1 phase with  $a_0 = 4.21$  Å, and AFM1 phase with  $a_0 = 4.25$  Å) and inner positions are obtained through full relaxation with a total energy tolerance  $10^{-6}$  eV. The SOC effect is self-consistently included. Modified Becke-Johnson (mBJ) is employed to correct the energy gap [53]. By considering the transition metal Mn in  $\text{MnBi}_2\text{Te}_4$ , LDA+U calculations are also performed to double check the results.

*Fitting parameters.* For the FM1 state,  $C = 0.0539$  eV,  $D_1 = -4.0339$  eVÅ<sup>2</sup>,  $D_2 = 4.4250$  eVÅ<sup>2</sup>,  $A_1 = 1.3658$  eVÅ,  $A_2 = 1.9985$  eVÅ,  $M_0^\gamma = 0.0307$  eV,

$B_1^\gamma = 4.2857$  eVÅ<sup>2</sup>,  $B_2^\gamma = 8.3750$  eVÅ<sup>2</sup>.  $A_3 = -0.5450$  eVÅ,  $A_4 = 1.1384$  eVÅ,  $M_0^\alpha = -0.1078$  eV,  $B_1^\alpha = 0.6232$  eVÅ<sup>2</sup>,  $B_2^\alpha = 0.6964$  eVÅ<sup>2</sup>,  $M_0^\beta = -0.0880$  eV,  $B_1^\beta = 2.7678$  eVÅ<sup>2</sup>, and  $B_2^\beta = 1.9650$  eVÅ<sup>2</sup>.

For the AFM1 state,  $C' = -0.0048$  eV,  $D_1' = 2.7232$  eVÅ<sup>2</sup>,  $D_2' = 17.0000$  eVÅ<sup>2</sup>,  $A_1' = 2.7023$  eVÅ,  $A_2' = 3.1964$  eVÅ,  $M_0' = -0.1165$  eV,  $B_1' = 11.9048$  eVÅ<sup>2</sup>, and  $B_2' = 9.4048$  eVÅ<sup>2</sup>.

We are grateful to Ke He for stimulating discussions. This work is supported by the Natural Science Foundation of China (Grant No. 11674165, 11774065, 11834006), the Fok Ying-Tong Education Foundation of China (Grant No. 161006), the National Key Research Program of China under Grant No. 2016YFA0300703, the Natural Science Foundation of Shanghai (Grant No. 17ZR1442500), the Open Research Fund Program of the State Key Laboratory of Low-Dimensional Quantum Physics (Contract No. KF201606), and by Fudan University Initiative Scientific Research Program.

*Note added:* Recently, we learned of the experimental paper in the same material by He *et al* [54].

\* zhanghj@nju.edu.cn

† wjingphys@fudan.edu.cn

- [1] M. Z. Hasan and C. L. Kane, *Rev. Mod. Phys.* **82**, 3045 (2010).
- [2] X.-L. Qi and S.-C. Zhang, *Rev. Mod. Phys.* **83**, 1057 (2011).
- [3] C.-K. Chiu, J. C. Y. Teo, A. P. Schnyder, and S. Ryu, *Rev. Mod. Phys.* **88**, 035005 (2016).
- [4] N. P. Armitage, E. J. Mele, and A. Vishwanath, *Rev. Mod. Phys.* **90**, 015001 (2018).
- [5] C. L. Kane and E. J. Mele, *Phys. Rev. Lett.* **95**, 226801 (2005).
- [6] B. A. Bernevig, T. L. Hughes, and S.-C. Zhang, *Science* **314**, 1757 (2006).
- [7] M. König, S. Wiedmann, C. Brüne, A. Roth, H. Buhmann, L. Molenkamp, X.-L. Qi, and S.-C. Zhang, *Science* **318**, 766 (2007).
- [8] X. Qian, J. Liu, L. Fu, and J. Li, *Science* **346**, 1344 (2014).
- [9] Y. Xia, D. Qian, D. Hsieh, L. Wray, A. Pal, H. Lin, A. Bansil, D. Grauer, Y. S. Hor, R. J. Cava, and M. Z. Hasan, *Nature Phys.* **5**, 398 (2009).
- [10] H. Zhang, C.-X. Liu, X.-L. Qi, X. Dai, Z. Fang, and S.-C. Zhang, *Nature Phys.* **5**, 438 (2009).
- [11] Y. L. Chen, J. G. Analytis, J. H. Chu, Z. K. Liu, S. K. Mo, X. L. Qi, H. J. Zhang, D. H. Lu, X. Dai, Z. Fang, S. C. Zhang, I. R. Fisher, Z. Hussain, and Z. X. Shen, *Science* **325**, 178 (2009).
- [12] H. Weng, C. Fang, Z. Fang, B. A. Bernevig, and X. Dai, *Phys. Rev. X* **5**, 011029 (2015).
- [13] S.-M. Huang, S.-Y. Xu, I. Belopolski, C.-C. Lee, G. Chang, B. Wang, N. Alidoust, G. Bian, M. Neupane, C. Zhang, S. Jia, A. Bansil, H. Lin, and M. Z. Hasan, *Nature Commun.* **6**, 7373 (2015).
- [14] A. A. Soluyanov, D. Gresch, Z. Wang, Q. Wu, M. Troyer,

- X. Dai, and B. A. Bernevig, *Nature* **527**, 495 (2015).
- [15] S.-Y. Xu, I. Belopolski, N. Alidoust, M. Neupane, G. Bian, C. Zhang, R. Sankar, G. Chang, Z. Yuan, C.-C. Lee, S.-M. Huang, H. Zheng, J. Ma, D. S. Sanchez, B. Wang, A. Bansil, F. Chou, P. P. Shibayev, H. Lin, S. Jia, and M. Z. Hasan, *Science* **349**, 613 (2015).
- [16] B. Q. Lv, H. M. Weng, B. B. Fu, X. P. Wang, H. Miao, J. Ma, P. Richard, X. C. Huang, L. X. Zhao, G. F. Chen, Z. Fang, X. Dai, T. Qian, and H. Ding, *Phys. Rev. X* **5**, 031013 (2015).
- [17] F.-f. Zhu, W.-j. Chen, Y. Xu, C.-l. Gao, D.-d. Guan, C.-h. Liu, D. Qian, S.-C. Zhang, and J.-f. Jia, *Nature Mat.* **14**, 1020 (2015).
- [18] L. Lu, J. D. Joannopoulos, and M. Soljačić, *Nature Photon.* **8**, 821 (2014).
- [19] J. Ruan, S.-K. Jian, H. Yao, H. Zhang, S.-C. Zhang, and D. Xing, *Nat. Commun.* **7**, 11136 (2016).
- [20] B. Bradlyn, J. Cano, Z. Wang, M. G. Vergniory, C. Felser, R. J. Cava, and B. A. Bernevig, *Science* **353**, aaf5037 (2016).
- [21] Z. Wang, A. Alexandradinata, R. J. Cava, and B. A. Bernevig, *Nature* **532**, 189 (2016).
- [22] B. Lv, Z.-L. Feng, Q.-N. Xu, X. Gao, J.-Z. Ma, L.-Y. Kong, P. Richard, Y.-B. Huang, V. Strocov, C. Fang, *et al.*, *Nature* **546**, 627 (2017).
- [23] H. Zhou, C. Peng, Y. Yoon, C. W. Hsu, K. A. Nelson, L. Fu, J. D. Joannopoulos, M. Soljačić, and B. Zhen, *Science* **359**, 1009 (2018).
- [24] S. Wu, V. Fatemi, Q. D. Gibson, K. Watanabe, T. Taniguchi, R. J. Cava, and P. Jarillo-Herrero, *Science* **359**, 76 (2018).
- [25] T. Zhang, Y. Jiang, Z. Song, H. Huang, Y. He, Z. Fang, H. Weng, and C. Fang, *ArXiv e-prints*: , 1807.08756 (2018).
- [26] F. Tang, H. C. Po, A. Vishwanath, and X. Wan, *ArXiv e-prints*: , 1807.09744 (2018).
- [27] M. G. Vergniory, L. Elcoro, C. Felser, B. A. Bernevig, and Z. Wang, *ArXiv e-prints*: , 1807.10271 (2018).
- [28] C.-Z. Chang, J. Zhang, X. Feng, J. Shen, Z. Zhang, M. Guo, K. Li, Y. Ou, P. Wei, L.-L. Wang, Z.-Q. Ji, Y. Feng, S. Ji, X. Chen, J. Jia, X. Dai, Z. Fang, S.-C. Zhang, K. He, Y. Wang, L. Lu, X.-C. Ma, and Q.-K. Xue, *Science* **340**, 167 (2013).
- [29] R. S. K. Mong, A. M. Essin, and J. E. Moore, *Phys. Rev. B* **81**, 245209 (2010).
- [30] X. Wan, A. M. Turner, A. Vishwanath, and S. Y. Savrasov, *Phys. Rev. B* **83**, 205101 (2011).
- [31] G. Xu, H. Weng, Z. Wang, X. Dai, and Z. Fang, *Phys. Rev. Lett.* **107**, 186806 (2011).
- [32] P. Tang, Q. Zhou, G. Xu, and S.-C. Zhang, *Nature Phys.* **12**, 1100 (2016).
- [33] G. Hua, S. Nie, Z. Song, R. Yu, G. Xu, and K. Yao, *ArXiv e-prints*: , 1801.02806 (2018).
- [34] X.-L. Qi, T. L. Hughes, and S.-C. Zhang, *Phys. Rev. B* **78**, 195424 (2008).
- [35] R. Yu, W. Zhang, H.-J. Zhang, S.-C. Zhang, X. Dai, and Z. Fang, *Science* **329**, 61 (2010).
- [36] L. Šmejkal, Y. Mokrousov, B. Yan, and A. H. MacDonald, *Nature Phys.* **14**, 242 (2018).
- [37] R. Li, J. Wang, X. L. Qi, and S. C. Zhang, *Nature Phys.* **6**, 284 (2010).
- [38] L. Šmejkal, J. Železný, J. Sinova, and T. Jungwirth, *Phys. Rev. Lett.* **118**, 106402 (2017).
- [39] J. Wang, *ArXiv e-prints*: , 1701.00896 (2017).
- [40] H. Zhang, J. Wang, G. Xu, Y. Xu, and S.-C. Zhang, *Phys. Rev. Lett.* **112**, 096804 (2014).
- [41] D. S. Lee, T.-H. Kim, C.-H. Park, C.-Y. Chung, Y. S. Lim, W.-S. Seo, and H.-H. Park, *CrystEngComm* **15**, 5532 (2013).
- [42] M. M. Otrokov, T. V. Menshchikova, M. G. Vergniory, I. P. Rusinov, A. Y. Vyazovskaya, Y. M. Koroteev, G. Bihlmayer, A. Ernst, P. M. Echenique, A. Arnau, and E. V. Chulkov, *2D Mater.* **4**, 025082 (2017).
- [43] L. Fu and C. L. Kane, *Phys. Rev. B* **76**, 045302 (2007).
- [44] R. Yu, X. L. Qi, A. Bernevig, Z. Fang, and X. Dai, *Phys. Rev. B* **84**, 075119 (2011).
- [45] J. Wang, B. Lian, X.-L. Qi, and S.-C. Zhang, *Phys. Rev. B* **92**, 081107 (2015).
- [46] M. Mogi, M. Kawamura, R. Yoshimi, A. Tsukazaki, Y. Kozuka, N. Shirakawa, K. S. Takahashi, M. Kawasaki, and Y. Tokura, *Nature Mater.* **16**, 516 (2017).
- [47] M. Mogi, M. Kawamura, A. Tsukazaki, R. Yoshimi, K. S. Takahashi, M. Kawasaki, and Y. Tokura, *Sci. Adv.* **3**, eaao1669 (2017).
- [48] D. Xiao, J. Jiang, J.-H. Shin, W. Wang, F. Wang, Y.-F. Zhao, C. Liu, W. Wu, M. H. W. Chan, N. Samarth, and C.-Z. Chang, *Phys. Rev. Lett.* **120**, 056801 (2018).
- [49] H. Jin, J.-H. Song, A. J. Freeman, and M. G. Kanatzidis, *Phys. Rev. B* **83**, 041202 (2011).
- [50] M. Wuttig and N. Yamada, *Nature Mater.* **6**, 824 (2007).
- [51] G. Kresse and J. Hafner, *Phys. Rev. B* **47**, 558 (1993).
- [52] G. Kresse and D. Joubert, *Phys. Rev. B* **59**, 1758 (1999).
- [53] F. Tran and P. Blaha, *Phys. Rev. Lett.* **102**, 226401 (2009).
- [54] K. He *et al.*, (to be published).